Seismic evidence for small-scale heterogeneity throughout the Earth's mantle

Michael A. H. Hedlin, Peter M. Shearer & Paul S. Earle

Institute of Geophysics and Planetary Physics, University of California, San Diego, La Jolla, California 92093-0225, USA

Details in the amplitude structure of short-period precursors to the seismic core phase PKP can be used to constrain the depth extent of mantle scattering. The simplest model consistent with the observations invokes small (~8 km), weak (r.m.s. velocity perturbations of 1%), random heterogeneities uniformly distributed throughout the mantle. The data do not support previously proposed models that place an increase in the concentration of scattering sites near the base of the mantle, and instead place an upper limit on the amplitude of any short-wavelength topography at the core–mantle boundary.

Seismic energy scattered from small-scale wave-velocity perturbations in the Earth generally arrives in the coda following the major seismic phases as the ray paths of the scattered waves have longer travel times than the direct arrivals. Possible weak scattering from deep structures is normally obscured by the much stronger scattering that results from near-surface crustal scattering and reverberation. However, the sharp velocity decrease at the core–mantle boundary (CMB) creates unusual ray geometries in which deep scattered energy can arrive before any of the major phases, providing a unique window into the small-scale structure of the deep Earth. The resulting faint short-period precursors to the earliest branch of PKP were first observed by Gutenberg and Richter[1], and there has been a continuing debate about their origin and what they imply about the Earth's velocity structure. Early hypotheses included diffraction of PKP at the CMB[2], refraction in the inner core[3], and reflection or refraction of PKP at transition layers between the inner and outer cores[4,5]. But it is now generally accepted that the precursors result from scattering of PKP off volumetric heterogeneities in the lowermost mantle and/or topography on the CMB[6,7], and this interpretation has been supported by analyses of the travel times, amplitudes, slownesses, and frequency content of precursors recorded by arrays of seismometers[8–11].

Researchers have modelled the amplitude and range dependence of the precursors by assuming statistical models of small-scale velocity heterogeneity. Although some of the older studies suggested that the scattering region extends at least 600–900 km above the CMB with velocity perturbations of a few per cent of more[11,12], other analyses indicated that the data could be explained with much thinner layers within the D″ region at the base of the mantle[13] or by short-wavelength CMB topography[14]. Recent studies have focused on the CMB region as the source of the scattering, suggesting that the data could be explained equally well by either 0.5–1.0% r.m.s. velocity perturbations in a 200-km-thick layer at the base of the mantle, or by CMB topography with r.m.s. height of about 300 m (refs 15, 16).

Resolving the location and nature of the scatterers is important because they provide some of the best constraints on small-scale heterogeneity in the deep Earth. But several significant issues remain unresolved, including the relative importance of topographic versus volume scattering, the scale and strength of the irregularities, the depth extent of any mantle heterogeneity and the possibility of lateral variations in the scattering strength. Here we present a detailed image of the time- and range-dependence of PKP precursor amplitudes, obtained by stacking 1,600 global seismograms. Modelling of these observations suggests that the precursors are caused by scattering from small-scale heterogeneity throughout most of the mantle. Some scattering from the CMB region is required to explain the onset of the precursors, but the CMB scattering appears no stronger than that occuring in the rest of the mantle. Velocity perturbations are about 1% at correlation scale lengths of 8 km. These results support models of small-scale compositional heterogeneity in the mantle[17–19].

PKP precursors

Figure 1 shows ray paths and travel-time curves for PKP and the region for which precursors may be observed. As hypothesized by Haddon[6], the earliest-arriving inner core branch (PKP_{df}) plays no role in the generation of these precursors but simply provides a reference phase for the earliest scattered waves to precede. The precursive arrivals stem from scattering off irregularities at the CMB or within the mantle, which deflect the ray paths of the mantle phase P to the outer-core phases PKP_{ab} and PKP_{bc}. Scattered energy is able to precede the df branch because of the unusual ray geometries arising from the sharp drop in P-wave velocity at the CMB. The earliest possible arrivals at any range are caused by scattering at the CMB; energy scattered above the CMB must arrive later.

Figure 2 shows examples of PKP precursors observed on individual seismograms between 118° and 145° range. The traces show increasing precursor amplitudes with increasing range. The time spanned by the precursor wavetrains reaches a maximum of roughly 18 s at 130° range. By 144.6° there is no evidence of any signal preceding PKP_{df}. The df coda amplitudes vary in a similar fashion, increasing with increasing range until the final trace at 144.6°.

Global average precursor amplitudes

From the on-line waveform archive of the Incorporated Research Institutions in Seismology (IRIS), we selected 1,600 broadband recordings of precursors made at source–receiver ranges between 118° and 145°. These traces are culled from a much larger set by using only those traces that exhibit stationary and low levels of noise. No consideration is made of the apparent presence or absence of precursors to avoid biasing our estimates of average precursor amplitudes. Next, we bandpass-filter each trace, compute its envelope function, and adjust its amplitude downward by an amount determined by the average energy level of the noise. Finally we align the records on the PKP_{df} arrival, correct the range for the effect of variable source depth, and stack the envelope functions in 1.5-s time bins and 1° range bins, with a weighting that gives preference to

those traces with the highest signal-to-noise ratios. We estimate error bounds on the stack using a bootstrap technique[20] in which we repeat the stack many times for random samples of our data.

The resulting stack, $S(r,t)$, shown in Figs 3 and 4, reveals a clear increase in precursor amplitude with increasing range and with increasing time. The correspondence between the onset of energy and the minimum travel-time curve for CMB scattering agrees with previous results[7], and suggests that some contributions are coming from the depth of the CMB. It seems likely that the signal onset continues to track the CMB scattering curve below 125°, but this is difficult to resolve because of low precursor energy levels.

Modelling precursor amplitudes

Our primary goal is to model the amplitudes in this stack to determine the depth range of the scatterers that contribute to the PKP_{df} precursors. Factors that will affect precursor amplitudes include the intrinsic strength and scale of the heterogeneities, the volume of scattering, the amplitude of the primary wave and the scattering angle.

With ray-tracing we can identify the places in the Earth from which any point in the stack could have received scattered energy (assuming the Earth reference model PREM and single scattering). As an example of this (Fig. 5) we show scattering isotimes for PKP_{bc} for a grid of scatterers located on the CMB near the receiver with the energy being recorded at two stations (located 130° and 140° from the source). All the scatterers located on the "−5 s" isotime contours in the upper and lower left panels of this figure will contribute energy to the stack at $S(140, -5)$ and $S(130, -5)$ respectively.

Figure 5 demonstrates that a unique, one-to-one, association between points in the stack, $S(r,t)$, and specific scatterers within the Earth cannot be made. At any range the energy which is associated with the most limited ambiguity is that which arrives first. As shown by the curves in Fig. 3, the earliest possible arrivals must have been

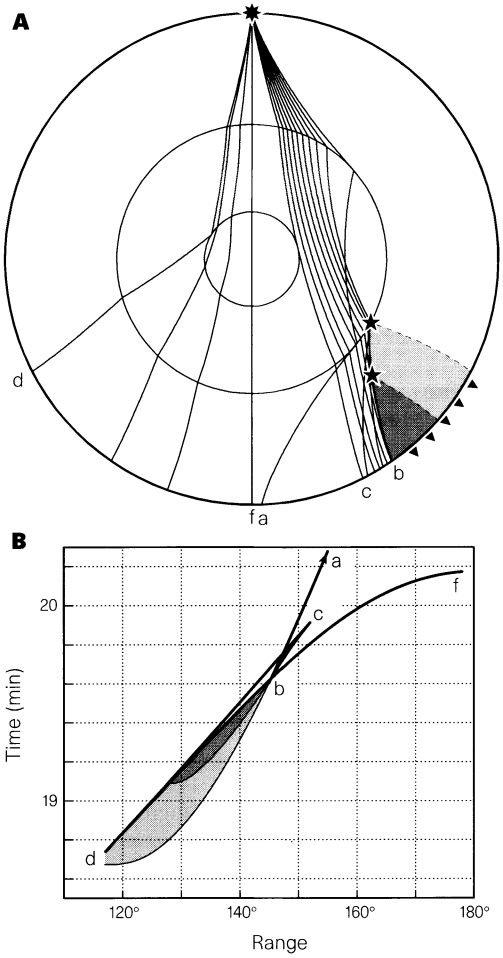

Figure 1 A, Ray paths of the different branches of PKP. The ab branch turns near the middle of the outer core, the bc branch turns just above the inner core, the cd branch is reflected from the inner-core boundary and the df branch turns within the inner core. Two scatterers (denoted by five-pointed stars) on the CMB and in the mantle near the receiver give rise to precursors that traverse the shaded regions. Although we have depicted PKP to P scattering into the shaded region on the receiver side of the travel path, precursors can also result from scattering on the source side (that is, from P to PKP). **B**, Travel-time curves for PKP are shown as heavy lines. The PKP precursors are observed to precede PKP_{df} by up to ~20 s at ranges less than the B caustic at 145° and are enriched in high frequencies. Energy scattered at the CMB can arrive as precursors to PKP in the lightly shaded region, scattered arrivals from a point in the mantle above the CMB can arrive in the darkly shaded area. Most of the scattered energy originates from the ab and bc branches near the B caustic.

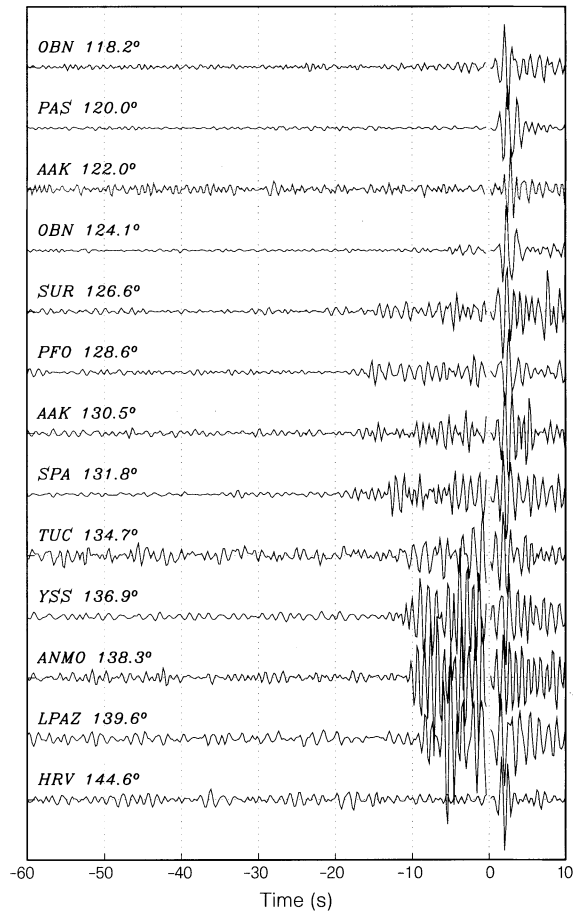

Figure 2 IRIS broadband recordings of PKP_{df} and preceding noise and precursors at ranges between 118° and 145°. These traces have been bandpass-filtered between 0.7 and 2.5 Hz and aligned on the PKP_{df} arrival. Amplitudes at negative times have been magnified by a factor of 7. The precursors are first visible in the OBN recording at 124.1° and last seen in the LPAZ recording at 139.6°. They become more energetic with increasing range. The earliest precursors precede PKP_{df} by 18 s (PFO at 128.6°). In some traces (for example, AAK at 122.0°) faint precursors may be obscured by pre-event noise.

scattered from the depth of the CMB. Later arrivals are associated with progressively more ambiguity as to the depth of scattering, because they represent a sum of energy scattered over a depth interval between the CMB and a shallower depth.

These ray-tracing results can also be used to compute the scattering angles (the angle by which the energy was diverted from its original path). In Fig. 5 we plot the PKP_{bc} scattering angles for CMB scatterers at 130° and 140° range. The scattering angle increases strongly with decreasing range, and also increases with increasing time and with the distance of the scatterer above the CMB. The increase in precursor amplitudes versus range is primarily due to the change in scattering angle, with stronger scattering occurring at smaller angles.

To model our observations, we assume that the precursors are due to the propagation of PKP through a random, inhomogeneous medium and use Chernov's acoustic scattering theory[21] adapted to elastic media[13]. To simplify the analysis we assume that the mantle behaves like a Poisson solid, that the random perturbations in velocity have an exponential autocorrelation function[22], and that we can neglect the influence of multiple scattering[23]. With these assumptions, the average scattered power is given by:

$$\langle |\Phi_s(\theta)|^2 \rangle = \frac{2k^4a^3\tilde{\alpha}^2VA^2}{\pi r^2} \frac{\frac{1}{4}[\cos(\theta)+\frac{1}{3}+\frac{2}{3}\cos^2(\theta)]^2}{[1+4k^2a^2\sin^2(\theta/2)]^2} \quad (1)$$

where θ is the scattering angle, A is the incident wave amplitude, V is the volume of scattering, $\tilde{\alpha}$ is the r.m.s. velocity perturbation $(\delta\alpha/\alpha_o)$, k is the wavenumber (ω/α_o), a is the characteristic scale length and r is the scatterer-to-receiver distance. Through numerical integration we can use this formula to obtain the predicted energy envelope of the precursor wavetrain. We compute k from the dominant 1.3-Hz frequency of our data and the P-wave velocity at the scattering depth. The $1/r^2$ factor is replaced by the geometric spreading factors and CMB transmission coefficients for the source–scatterer and scatterer–receiver ray paths. We use simple ray theory to compute these spreading factors; more sophisticated analysis has shown that this is adequate for this problem[23].

We include the contributions from both PKP_{ab} and PKP_{bc} scattering. To compare with our observations, we normalize our synthetic wavetrain to the predicted peak amplitude of $PKP_{df} + PKP_{cd}$, by raytracing through PREM and assuming an inner core Q of 360 (ref. 24). The choice of inner-core Q is significant as it affects the dependence of PKP_{df} amplitude on range. As we will see in the next section, the range dependence of the precursor-to-PKP_{df} amplitude ratio largely determines which scale length provides the best match between synthetics and data. Note that equation (1) predicts that the scattering becomes strongly forward for large-scale heterogeneity ($ka \gg 1$), and that the precursor amplitude varies directly with the velocity perturbation.

The depth extent of mantle scattering

To constrain the depth range of any mantle scattering, we divide the mantle into thin (20-km) layers, from the CMB to the crust, and

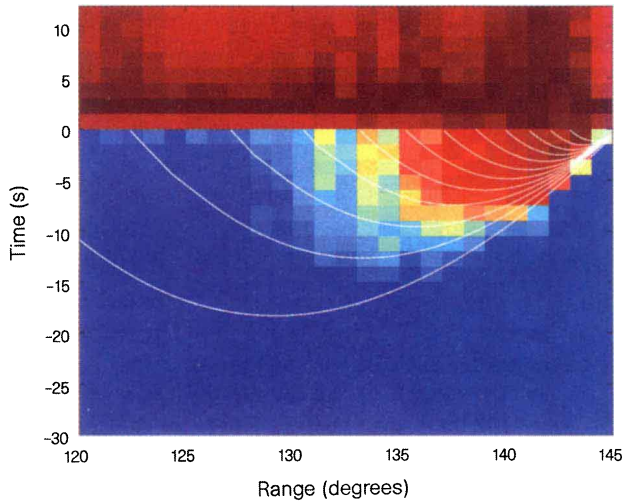

Figure 3 Average amplitude of PKP_{df} and its precursors at ranges from 120° to 145°, resulting from a stack of 1,600 short-period seismograms. Time is relative to the onset of PKP_{df}. Note the gradual growth in precursor amplitudes with increasing time and range. Included in this display are minimum travel-time curves for scattered arrivals calculated using the PREM velocity model[38]. The lowest curve indicates the minimum travel time of energy single-scattered at the CMB (no energy scattered at the CMB could arrive earlier than the lowest curve). The other curves represent the minimum travel time for scattering occurring at 200-km intervals up into the mantle, with the last curve representing scattering 2,200 km above the CMB. These curves show that at short ranges and early times only scatterers close to the CMB can cause precursors, while at longer ranges and later times an increasing fraction of the mantle can contribute to the precursor wavetrain. For example, no precursors recorded at ranges less than 127° can result from scattering more than 400 km above the CMB, whereas at 143° the last part of the precursor wavetrain before the PKP_{df} arrival could contain contributions from scattering up to 2,200 km above the CMB.

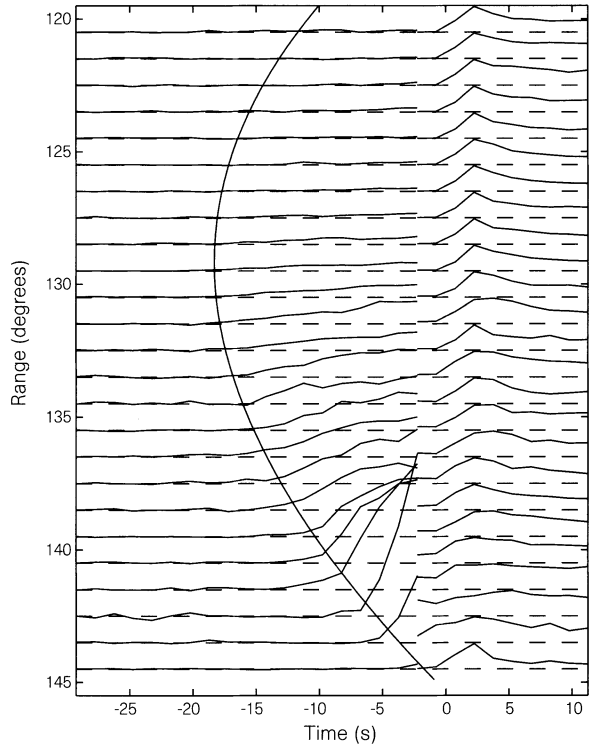

Figure 4 Average precursor amplitudes as a function of time and source–receiver range as obtained from a waveform stack of 1,600 seismograms. Times are relative to the onset of PKP_{df}. Each stacked trace is normalized to the peak PKP_{df} amplitude (see at about 2 s); amplitudes at negative times in this plot are multiplied by 10 to enhance the visibility of the precursors. The theoretical onset time from the PREM velocity model for single-scattering at the CMB is shown as the curved line. Note the increase in precursor levels with range and the gradual increase in precursor energy on each trace up to the time of the PKP_{df} arrival. It is this time dependence in the precursor amplitudes that favours models of scattering distributed throughout the mantle. At the longer ranges the stacked precursor envelope tends to begin rising somewhat earlier than the PREM predicted onset time. Although some of this is due to the finiteness of our binning scheme, it may also reflect slight inaccuracies in the PREM model. Predicted PKP_{df} precursor onset times vary by up to several seconds between different reference velocity models (for example, PREM; iasp91[39]; sp6[40]). We account for these uncertainties by permitting small time shifts in our modelling procedure (see text).

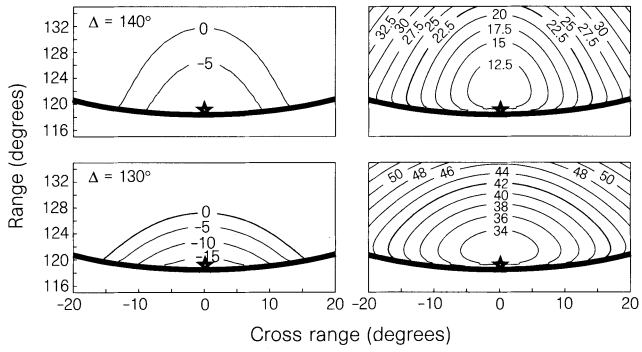

Figure 5 The two contoured plots on the left show residual travel times for energy single-scattered from PKP_{bc} to P at the CMB when compared with PKP_{df} arrival times. At a range, Δ, of 130° the first arriving energy is expected 18.45 s before PKP_{df} and is scattered from a point adjacent to the B caustic in the diametral plane of the source and receiver (star at a cross-range of 0° in lower left figure). The curves labelled "0" indicate the locations from which single-scattered energy will arrive at the receiver at the same time as PKP_{df}. On the conjugate side of the travel path there are equivalent contours which describe the isotimes associated with near-source scattering. These curves are the traces, on the CMB, of three-dimensional isotime surfaces which extend into the mantle. The two plots on the right show the PKP_{bc}-to-P scattering angles at the CMB for the same grid of scatterers and receiver locations. The greatest scattering angles are associated with out-of-plane scattering. Scattering angles are much larger at shorter ranges and generally increase with time at a given range.

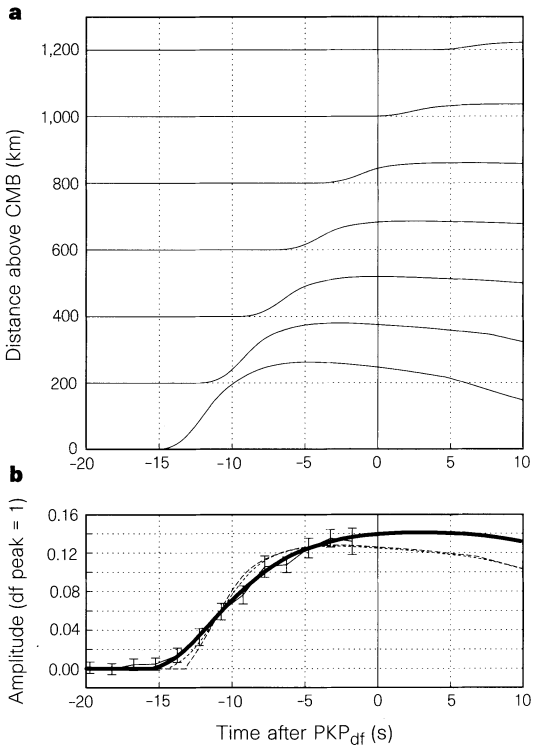

Figure 6 a, Scattering energy kernels for random mantle velocity perturbations at seven depths ranging from the CMB up to 1,200 km above it. The kernels were calculated assuming an exponential autocorrelation function with an 8-km scale and a source–receiver range of 135.5°, and have been convolved with an empirical source-time function derived from the PKP_{df} arrivals in the stack (Fig. 4). The energy in the source-time function is concentrated in the earliest 6 s but spans 20 s to include the coda following the main arrival (probably caused by near source and receiver crustal resonance). The square root of a sum of these energy kernels can be used to model the data amplitudes displayed in Figs 3 and 4. **b**, Plot showing data fitting. An unweighted sum of all kernels yields the solid curve. This curve tracks the data much more closely than the curves that result from models that allow scattering only in the lower 200 km of the mantle (short dashes) and in the lowermost 20 km of the mantle (long dashes). The latter two models predict abrupt onsets and a levelling-off in amplitude before the PKP_{df} arrival. One standard error bars are shown for the data curve; these are estimated through a random resampling of the seismograms.

calculate the response of each individual layer to the incident wavefield. The statistics of the heterogeneity are invariant within each layer and are allowed to change only in strength between layers. In Fig. 6 we show these responses, or kernels, for seven of these layers ranging in depth from the CMB to 1,200 km above. These were calculated assuming an exponential autocorrelation function with an 8 km scale-length and a source–receiver range of 135.5°. We find that the largest and earliest contributions will come from the deepest layers and that, at this range, the precursors must originate from a volume within 1,000 km of the CMB. Scattering that occurs at higher levels will arrive after PKP_{df} and be obscured by the coda of this phase. The amplitude decay with time present in each kernel is largely due to an increase in the scattering angle.

By summing the energy of different combinations of these kernels we can explore the effect of scattering within different mantle depth intervals. Figure 6 shows the fit obtained for whole-mantle scattering (solid line), compared to scattering restricted to the lowermost 200 km (short dashed line) and lowermost 20 km (long dashed line). We have adjusted the velocity perturbation and allowed a small time shift (to account for the uncertainties in the reference velocity model) to achieve the best fit. In this case we find that the whole-mantle scattering model provides the best match to the data. The two models that allow heterogeneities only at the CMB (acting as a proxy for topography) or in a 200-km-thick D″ layer provide a poorer fit to the data, in that they predict a rapid increase in amplitude that tapers off just before the arrival of PKP_{df}. Only the full-mantle model allows significant contributions to the precursor wavetrain to arrive late and thus produces a curve which rises gradually and continuously until well after the arrival of PKP_{df}.

This behaviour is also seen in our observations at other ranges (Fig. 4). Precursor amplitudes increase gradually with time until the PKP_{df} arrival and do not exhibit a sharp onset that would be diagnostic of scattering restricted to the lowermost mantle. In Fig. 7 we plot our theoretical fits to 11 independent precursor stacks at ranges between 130° and 140°, showing that consistently the best fit is provided by the model that assumes uniform scattering intensity throughout the mantle. Only this model matches the emergent onset of the precursors and the continual rise in energy with time present in all bins. Considering the 143 data points in Fig. 7 within 20 s of the PKP_{df} onset; a χ^2 test returns values of 172.3, 286.0 and 373.0 for the whole-mantle, D″ and CMB models, respectively, indicating that the whole-mantle model fits the data within the standard errors (significant at the 95% confidence level), while the other models fit the observations much less well. The r.m.s. velocity

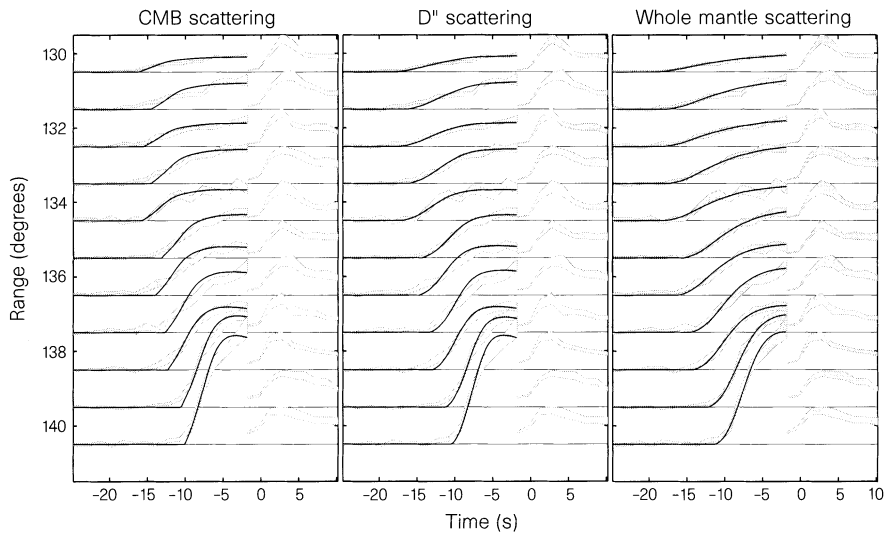

Figure 7 Observed average PKP_{df} precursor amplitudes at ranges between 130° and 141° compared to theoretical predictions of three different models of mantle heterogeneity. The data and their standard errors are indicated with the grey shaded regions (compare with Figs 3 and 4). The left-hand panel shows the best fit to the data achieved with a model in which scattering is restricted to the core-mantle boundary. The centre panel indicates the fit when scattering is permitted within the lowermost 200 km of the mantle (that is, within the D″ region), and the right-hand panel shows the fit obtained from a model in which the scattering strength is uniform throughout the mantle. Only the whole-mantle model provides an adequate overall fit to the data; the other models do not match the emergent onset of the precursors and their steady increase in amplitude until the main PKP_{df} arrival. This conclusion is supported by χ^2 tests of the significance of the theoretical fits–only the whole-mantle fits the data within their standard errors.

contrast required to bring the full-mantle curves into agreement with the stack averages just over 1%. In several of the bins (for example 134.5°) the stack contains small-scale structure that is not reproduced by any of the models. In addition, several of the bins require larger velocity contrasts (the scatter was from 0.8% to 2.0%, with the amplitudes greatest in the bin spanning 131° to 132°). Because of clustering of events, some bins are dominated by certain stations or source regions; thus these anomalies may be caused by lateral variations in scattering strength in the mantle. Although this analysis shows that the CMB and D″ scattering models (similar to those proposed in the past to explain PKP precursor data) are inconsistent with the observations, we cannot exclude the possibility that more complicated models, perhaps involving multiple scattering, might exist that could explain the data without requiring mid-mantle scattering.

We prefer the 8-km scale length as it gives the best overall fit to the observations. Different scale lengths (4–16 km) can produce acceptable fits to the data, but require that the velocity contrast be strongly dependent on range. This finding is dependent on several assumptions, most notably the Q of the inner core (changing Q would favour a different scale length). However, any uncertainty in the scale length does not affect our conclusion regarding whole-mantle scattering, as the CMB and D″ scattering predictions (shown in Fig. 7) do not produce adequate fits to the data at any scale length. In addition to the exponential autocorrelation results shown here, we have also experimented with a gaussian autocorrelation model[22], and find that it gives very similar results, again favouring whole-mantle scattering. Although other possible models of random heterogeneity could be considered, all will generally predict a decrease in scattered amplitude with increasing scattering angle at the low angles involved. As scattering angle increases with time at each range (Fig. 5), shallow heterogeneity (and the late precursors it provides) is required to reproduce the emergent precursor amplitudes and continuous energy increase seen in the observations.

The principal advantage of our analysis over earlier studies of PKP precursors is that we are able to resolve the time dependence of the average precursor amplitude. This time dependence is critical to resolving the question of the depth extent of the scatterers. Previous analyses of these precursors focused mainly on modelling the range- and scattering-angle dependence of precursor amplitudes, and thus could not unambiguously determine the depth of the scattering. Our ability to image scattering in the upper mantle (above about 1,500 km depth) is limited as only a small part of the image constrains this part of the model. However, we see no evidence that scattering decreases in the upper mantle and prefer the uniform scattering model as the simplest explanation for our observations. Although more complicated models could certainly be devised, involving depth dependence in the strength and scale length of the scatterers, it is apparent that no laterally uniform model in which scattering is restricted to the lowermost mantle will fit the observations. There is no evidence from PKP precursors for an increase in small-scale heterogeneity near the CMB.

Although the focus of this Article has been PKP scattering, widespread mantle heterogeneities will cause scattering of other seismic phases and this provides a possible way to test our proposed model. Preliminary calculations of PP scattering indicate that our whole-mantle model predicts scattered arrivals between diffracted P and PP, but at such small amplitudes that these PP precursors would not be observable in our data stacks.

An important question still remains. How much topography on the CMB do the data allow? To place an upper bound on CMB r.m.s. topography we calculate the scattering response of an Earth model that contains no mantle volume heterogeneities except for a thin layer of heterogeneities at the CMB (serving as a proxy for topography). By scaling the strength of heterogeneities in this thin layer we can find the maximum velocity contrast that is within the data confidence limits and then convert this contrast to the equivalent r.m.s. topography[15]. Considering all bins from 120.5° to 142.5° and a horizontal scale length of 8 km, we find that the smallest upper bound (yielded by the bin spanning 124° to 125°) is 300 m. This result represents a conservative limit on CMB r.m.s. topography as any contribution from mantle scattering would reduce the allowed topography. The implication of a fairly smooth CMB at small scales is consistent with observations of high-frequency core-reflected phases[25,26]. However, there remains evidence for at least some short-wavelength CMB topography from

PKKP precursor studies[27–29]. Our results also do not exclude the possibility of significant CMB topography at long wavelengths.

Geodynamical implications

By stacking a large set of global data, we have produced an image of PKP precursors that shows consistent patterns in the range- and time-dependence of the precursor amplitudes. The average precursor energy levels are emergent and increase gradually in amplitude up to the arrival of the main PKP_{df} phase. This behaviour is consistent with uniform scattering through the mantle, as models in which the scattering is restricted to the D″ region predict much more impulsive precursor wavetrains. The observations do not favour a significant contribution to the precursors from CMB topography, and limit allowed relief to less than 300 m at short scales. Other than marking the base of the mantle, there is nothing in the data to suggest that there is anything special about the CMB region in regard to generating PKP precursors.

This contrasts with seismic results at longer wavelengths, where increasing evidence suggests that the D″ region is more heterogeneous than the mid-mantle[30–34]. Our results indicate mantle velocity perturbations close to 1% at correlation lengths of 8 km, close to the dominant wavelength of our data. Extensions of these results to other scale lengths require assumptions about the heterogeneity power spectrum that are difficult to verify due to the limited bandwidth in which the PKP precursors can be observed. At long wavelengths (>500 km), both global and regional seismic tomography studies indicate a sharp fall off in mantle heterogeneity with angular order[31,35] suggesting that the mantle becomes more homogenous at shorter scale lengths. Our results indicate that this fall off cannot be extrapolated to predict mantle heterogeneity at very short scale lengths.

If high frequency seismic waves are scattered throughout the mantle, then at least some of the high-frequency coda following major seismic arrivals at teleseismic distances is caused by mantle heterogeneity. However, this scattered energy may be difficult to isolate from the strong near-surface contributors to seismic coda. Our results support models containing small-scale compositional heterogeneity in the mantle[17–19]. Subducting oceanic lithosphere entrained by mantle convection provides a possible origin for this heterogeneity[17]; numerical convection experiments indicate that such heterogeneity could survive for billions of years due to imperfect mixing in the flow field[19,36]. Small-scale thermal anomalies seem a less probable source for scattering as they would quickly dissipate at short wavelengths and would have to be widespread and active on short timescales to explain our observations.

Although our focus here has been on global average precursor amplitudes, it is clear that scattering intensity varies on a regional scale. These variations are often seen on individual seismograms, with certain source or receiver regions consistently associated with more, or less, energy than the global average. Thus it is likely that some parts of the mantle scatter more strongly than the average values. We are currently attempting to characterize these intensity variations by back-propagating, or migrating, the recorded energy into the mantle[37]. □

Received 29 April 1996; accepted 24 March 1997.

1. Gutenberg, B. & Richter, C. F. On seismic waves: I. *Gerlands Beitr. z. Geophysik.* **43,** 56–133 (1934).
2. Bullen, K. E. & Burke-Gaffney, T. N. Diffracted seismic waves near the PKP caustic. *Geophys. J. Int.* **1,** 9–17 (1958).
3. Gutenberg, B. The boundary of the Earth's inner core. *Eos* **38,** 750–753 (1957).
4. Bolt, B. A. Gutenberg's early *PKP* observations. *Nature* **196,** 122–124 (1962).
5. Sacks, I. S. & Saa, G. The structure of the transition zone between the inner core and the outer core. *Yb. Carnegie Inst. Wash.* **69,** 419–426 (1969).
6. Haddon, R. A. W. Corrugations on the CMB or transition layers between inner and outer cores? *Eos* **53,** 600 (1972).
7. Cleary, J. R. & Haddon, R. A. W. Seismic wave scattering near the core–mantle boundary: a new interpretation of precursors to *PKP. Nature* **240,** 549–551 (1972).
8. Doornbos, D. J. & Husebye, E. S. Array analysis of *PKP* phases and their precursors. *Phys. Earth Planet. Inter.* **5,** 387–399 (1972).
9. King, D. W., Haddon, R. A. W. & Cleary, J. R. Array analysis of precursors to *PKIKP,* in the distance range 129° to 142°. *Geophys. J. R. Astron. Soc.* **37,** 157–173 (1974).
10. Husebye, E. S., King, D. W. & Haddon, R. A. W. Precursors to *PKIKP* and seismic wave scattering near the mantle-core boundary. *J. Geophys. Res.* **81,** 1870–1882 (1976).
11. Doornbos, D. J. Characteristics of lower mantle inhomogeneities from scattered waves. *Geophys. J. R. Astron. Soc.* **49,** 541–542 (1976).
12. Doornbos, D. J. & Vlaar, N. J. Regions of seismic wave scattering in the Earth's mantle and precursors to *PKP. Nature* **243,** 58–61 (1973).
13. Haddon, R. A. W. & Cleary, J. R. Evidence for scattering of seismic *PKP* waves near the mantle-core boundary. *Phys. Earth Planet. Inter.* **8,** 211–234 (1974).
14. Doornbos, D. J. On seismic-wave scattering by a rough core-mantle boundary. *Geophys. J. R. Astron. Soc.* **53,** 643–662 (1978).
15. Bataille, K. & Flatte, S. M. Inhomogeneities near the core-mantle boundary inferred from short-period scattered *PKP* waves recorded at the global digital seismograph network. *J. Geophys. Res.* **93,** 15057–15064 (1988).
16. Bataille, K., Wu, R. S. & Flatte, S. M. Inhomogeneities near the core-mantle boundary evidenced from scattered waves: a review. *Pure Appl. Geophys.* **132,** 151–173 (1990).
17. Davies, G. F. Geophysical and isotopic constraints on mantle convection: an interim synthesis *J. Geophys. Res.* **89,** 6017–6040 (1984).
18. Davies, G. F. Mantle plumes, mantle stirring and hotspot chemistry. *Earth Planet. Sci. Lett.* **99,** 94–109 (1990).
19. Gurnis, M. & Davies, G. F. Mixing in numerical models of mantle convection incorporating plate tectonics. *J. Geophys. Res.* **91,** 6375–6395 (1986).
20. Efron, B. & Tibshirani, R. Statistical data analysis in the computer age. *Science* **253,** 390–395 (1991).
21. Chernov, L. A. *Wave Propagation in a Random Medium* (trans. Silverman, R. A.) (McGraw-Hill, New York, 1960).
22. Wu, R. S. & Aki, K. Elastic wave scattering by a random medium and the small-scale inhomogeneities in the lithosphere. *J. Geophys. Res.* **90,** 10261–10273 (1985).
23. Cormier, V. Time domain modeling of *PKIKP* precursors for constraints on the heterogeneity in the lowermost mantle. *Geophys. J. Int.* **212,** 725–736 (1995).
24. Bhattacharyya, J., Shearer, P. M. & Masters, G. Inner core attenuation from short-period *PKP(BC)* versus *PKP(DF)* waveforms. *Geophys. J. Int.* **114,** 1–11 (1993).
25. Menke, W. Few 5–20 km corrugations on the core-mantle boundary. *Geophys. Res. Lett.* **13,** 1501–1504 (1986).
26. Vidale, J. E. & Benz, H. M. A sharp and flat section of the core–mantle boundary. *Nature* **359,** 627–629 (1992).
27. Chang, A. C. & Cleary, J. R. Precursors to *PKKP Bull. Seismol. Soc. Am.* **68,** 1059–1079 (1978).
28. Chang, A. C. & Cleary, J. R. Scattered *PKKP*: further evidence for scattering at a rough core-mantle boundary. *Phys. Earth Planet. Inter.* **24,** 15–29 (1981).
29. Doornbos, D. J. The effect of a rough core-mantle boundary on *PKKP. Phys. Earth Planet. Inter.* **21,** 351–358 (1980).
30. Woodward, R. L. & Masters, T. G. Lower-mantle structure from *ScS-S* differential travel times. *Nature* **352,** 231–233 (1991).
31. Su, W.-J. & Dziewonski, A. M. Predominance of long-wavelength heterogeneity in the mantle. *Nature* **352,** 121–126 (1991).
32. Masters, T. G., Johnson, S., Laske, G. & Bolton, H. A shear-velocity model of the mantle. *Phil. Trans. R. Soc. Lond. A* **354,** 1–27 (1996).
33. Lay, T. Structure of the core-mantle transition zone: a chemical and thermal boundary layer. *Eos* **70,** 49, 54–55, 58–59 (1989).
34. Loper, D. E. & Lay, T. The core-mantle boundary region. *J. Geophys. Res.* **100,** 6397–6420 (1995).
35. Passier, M. L. & Sneider, R. K. On the presence of intermediate-scale heterogeneity in the mantle. *Geophys. J. Int.* **123,** 817–837 (1995).
36. Christensen, U. R. & Hofmann, A. W. Segregation of subducted oceanic crust in the convecting mantle. *J. Geophys. Res.* **99,** 19867–19884 (1994).
37. Hedlin, M. A. H., Shearer, P. M. & Earle, P. Imaging CMB scatterers through migration of GSN *PKPdf* precursor recordings. *Eos* **76,** F402 (1995).
38. Dziewonski, A. & Anderson, D. L. Preliminary reference earth model. *Phys. Earth Planet. Inter.* **25,** 297–356 (1981).
39. Kennett, B. L. N. (ed.) *IASPEI 1991 Seismological Tables* (Res. Sch. Earth Sci., Aust. Nat. Univ., Canberra, 1991).
40. Morelli, A. & Dziewonski, A. M. Body wave traveltimes and a spherically symmetric *P*- and *S*-wave velocity model. *Geophys. J. Int.* **112,** 178–194 (1993).

Acknowledgements. Data were collected by the IRIS Global Seismographic Network and obtained from the IRIS FARM. This work was supported by the US National Science Foundation.

Correspondence should be addressed to M.A.H.H. (e-mail: hedlin@ucsd.edu).